



Catalytic combustion of 1,2-dichlorobenzene at low temperature over Mn-modified Co_3O_4 catalysts



Ting Cai^a, Hao Huang^a, Wei Deng^a, Qiguang Dai^a, Wei Liu^b, Xingyi Wang^{a,*}

^a Lab for Advanced Materials, Research Institute of Industrial Catalysis, East China University of Science and Technology, Shanghai 200237, PR China

^b Shanghai Institute of Applied Physics Chinese Academy of Science, Shanghai 201800, PR China

ARTICLE INFO

Article history:

Received 25 July 2014

Received in revised form

23 September 2014

Accepted 18 October 2014

Available online 28 October 2014

Keywords:

1,2-Dichlorobenzene

Catalytic combustion

Manganese

Cobalt

Spinel

ABSTRACT

Mn-modified Co_3O_4 catalysts with spinel structure with various Co/Mn ratios prepared by co-precipitation method were characterized by XRD, Raman, TEM, HRTEM, XPS and H_2 -TPR, and used in catalytic combustion of 1,2-dichlorobenzene (*o*-DCB), as a model of dioxins. The results revealed that the catalyst with Co/Mn ratio of nine presented the highest activity with T_{90} of 347 °C and high stability at least 35 h at 3000 ppm *o*-DCB and 10% O_2 at $\text{GHSV} = 15,000 \text{ h}^{-1}$. High activity could be ascribed to synergistic effect between activation of *o*-DCB on Co²⁺ sites and oxidation by surface active oxygen from Co_3O_4 nano-particles. Additionally, 1,2,4-trichloro-benzene was formed over Co_3O_4 to a significant extent through the reaction of adsorbed Cl species with *o*-DCB, while the incorporation of Mn in Co_3O_4 can effectively retard chlorination of *o*-DCB. A possible reaction pathway for the catalytic combustion of *o*-DCB on Co_{x}Mn_y catalysts was also investigated by *in situ* FTIR spectroscopy.

© 2014 Published by Elsevier B.V.

1. Introduction

Chlorinated organic compounds in waste gases are released to the atmosphere from a wide range of industrial processes or the incineration of municipal and medical wastes. Among them, polychlorinated dibenzodioxins (PCDDs) and dibenzofurans (PCDFs) known as dioxins are chlorinated organic molecules belonging to the category of persistent organic pollutants (POPs) with high toxicity and carcinogenicity, able to persist in the ecosystem for several years [1]. Hence, stringent environmental regulations are in place in several countries limiting PCDD/PCDF emissions [2,3]. Various control methods have been designed and used [2,4], of which catalytic oxidation is the preferred approach [3,5,6]. Its major advantage is that oxidation can be effectively performed at temperatures between 250 and 550 °C, and very dilute pollutants which cannot be thermally combusted without additional fuel can be treated effectively by this way [7]. Another advantage is its excellent selectivity toward formation of the desired products such as carbon dioxide, HCl and water. Normally, considering PCDD/Fs' high toxicity and delicate manipulation in laboratories, model compounds have been used to evaluate the activity of catalysts in the majority of these studies. Monochlorobenzene (MCB) and 1,2-dichlorobenzene

(*o*-DCB) have been most frequently used, because of their structural similarity to PCDDs.

During the past decades, a number of catalyst systems for the total oxidation of chlorinated compounds have been reported. But most of them focused on three types of catalysts based on noble metals [3,6,7], transition metals [5,8,9] and zeolites [10–12]. The activity of noble metal catalysts was often very high, but they were susceptible to the deactivation by adsorption of HCl and Cl_2 , and were also sensitive to higher temperatures. The activity of zeolites was related to their acid properties. However, the formation of polychlorinated compounds and the deposition of coke on these acidic catalysts are yet to be solved out. Transition metal oxides, in general, were less active than noble metals but they can resist deactivation by chlorine poisoning to a larger extent [13]. And the use of transition metal catalysts can lower the cost because most of them are less expensive. Thus, there were few reports about transition metal oxides used for catalytic combustion of *o*-DCB in recent years, including $\text{V}_2\text{O}_5/\text{TiO}_2$ [2,4], $\text{CaCO}_3/\text{Fe}_2\text{O}_3$ [8], $\text{Fe}-\text{Ca}-\text{O}_x/\text{TiO}_2$ [14], TiO_2 -masked Fe_3O_4 [15] and so on. $\text{V}_2\text{O}_5/\text{TiO}_2$ prepared by a sol-gel method showed a very high activity and thermal stability for gas phase oxidation of *o*-DCB, but V_2O_5 is toxic and can cause secondary pollution. $\text{CaCO}_3/\text{Fe}_2\text{O}_3$ showed a considerable activity for catalytic combustion of *o*-DCB, but the activity was decreased in the presence of water. Therefore, development of catalysts having high catalytic performance and resistance to chlorine poisoning is of great interest.

* Corresponding author. Tel.: +86 21 64253372; fax: +86 21 64253372.

E-mail address: wangxy@ecust.edu.cn (X. Wang).

As a material with typical spinel structure, Co_3O_4 has attracted intensive attention due to its wide applications in catalysis [16,17]. Co_3O_4 consists of Co^{2+} at tetrahedral sites and Co^{3+} at octahedral sites. In principle, replacement of cobalt with other elements at octahedral sites can affect the binding strength of metal–oxygen, resulting in different adsorption energies for $-\text{OOH}$ species at catalytic sites [18]. The roles of octahedral and tetrahedral cobalt cations in the surface reactivity, thermal and electrical properties were investigated by the controlled insertion of iron into the lattice of cobalt oxide [19]. Appropriate incorporation of metal oxides may exhibit higher activity and thermal stability than the single oxides as recently reported. $\text{Co}_{3-x}\text{Fe}_x\text{O}_4$ [19], $\text{Mn}_x\text{Co}_{3-x}\text{O}_4$ [20,21], $\text{Co}_{3-x}\text{Cu}_x\text{O}_4$ [22], $\text{Zn}_x\text{Co}_{1-x}\text{Co}_2\text{O}_4$ [23] and NiO_x , CrO_x and Bi_2O_3 modified Co_3O_4 [24–26] presented higher active than pure Co_3O_4 during oxidation. $\text{Mn}_x\text{Co}_{3-x}\text{O}_4$ catalysts are low cost, environmentally friendly and highly active for the combustion of volatile organic compound (VOCs), such as *n*-hexane [27], methane [28,29] and formaldehyde [20]. The promotion of catalytic abilities was attributed to a favorable synergistic effect between manganese and cobalt oxides. Zhang [21] found that the stability of Co_3O_4 was also remarkably enhanced by the modification with MnO_x . To the best of our knowledge, however, the use of $\text{Mn}_x\text{Co}_{3-x}\text{O}_4$ to catalyze *o*-DCB oxidation has never been reported. In the present work, a series of $\text{Mn}_x\text{Co}_{3-x}\text{O}_4$ catalysts with spinel structure were prepared by co-precipitation method, and used in catalytic combustion of *o*-DCB. Our goal is to gain more insight into the surface chemistry during these processes as well as the correlation of the activity and stability of $\text{Mn}_x\text{Co}_{3-x}\text{O}_4$ catalysts to surface structure and performance.

2. Experimental

2.1. Catalyst preparation

Stoichiometric amounts of $\text{Co}(\text{NO}_3)_2 \cdot 6\text{H}_2\text{O}$ and 50% $\text{Mn}(\text{NO}_3)_2$ were first dissolved in 50 ml deionized water, and then an aqueous solution of Na_2CO_3 was added dropwise into the mixed aqueous solution under vigorous agitation. The temperature was kept at 80 °C and pH, at about 8.5 during the precipitation for 2 h. The resulted precipitates were collected and washed thoroughly with deionized water. All of catalyst precursors were dried at 110 °C overnight, then heated up to 500 °C with a heating rate of 1 °C min⁻¹ in static air, and finally calcined at 500 °C for 4 h. Catalysts were noted as Co_xMn_y in which x and y were based on Co and Mn mole number. For example, Co_5Mn_1 represents the catalyst with Co/Mn ratio of 5:1 (mol). Pure Co_3O_4 and MnO_x were also prepared by the similar procedures described above.

2.2. Catalysts characterization

The powder X-ray diffraction patterns (XRD) of samples were recorded on a Rigaku D/Max-rC powder diffractometer using Cu Ka radiation (40 kV and 100 mA). The diffractograms were recorded in the 2 θ range of 10–80 °C with a 2 θ step size of 0.01° and a step time of 10 s. The nitrogen adsorption and desorption isotherms were measured at –196 °C on an ASAP 2400 system in static measurement mode. Samples were out-gassed at 160 °C for 4 h before the measurement. Specific surface area was calculated using BET model. The chemical compositions of the prepared catalysts were determined by ICP-AES with the instrument model of Vanan 710. The residual amount of surface chloride species were determined by Energy Dispersive Spectrometer (EDS) of Falion. The transmission electron microscopy (TEM) images of powder samples were recorded on a JEM-1400 instrument operated at 120 kV. High-resolution transmission electron microscopic (HRTEM) images were taken on a JEM-2100 microscope that operated at 200 kV. The

XPS measurements were made on a VG ESCALAB MK II spectrometer by using Mg Ka (1253.6 eV) radiation as the excitation source. Charging of samples was corrected by setting the binding energy of adventitious carbon (C1s) at 284.6 eV. Powder samples were pressed into self-supporting disks, loaded into a sub-chamber, and evacuated to 10⁻⁹ mbar maintaining 4 h, prior to the measurements at 25 °C. Raman spectra were recorded on Via Reflex Laser Raman instrument, equipped with a CCD (charge coupled device) detector. The excitation source was the 514.5 nm line of Ar ion laser. The laser power was set at 3 mW. All data or results obtained from characterization tests are repeated basically three times. H_2 -temperature programming reduction (H_2 -TPR) was investigated by heating catalysts (100 mg) in H_2 (5 vol%) / Ar flow (30 ml min⁻¹) at a heating rate of 10 °C min⁻¹ from 50 to 750 °C. The hydrogen consumption was monitored by a gas chromatographs (GC) equipped with thermo-conductivity detector. Before the H_2 -TPR analysis, the samples were heated for 60 min in Ar flow at 300 °C. O_2 -TPD was carried out in a U-shaped quartz tube and the desorption signal of oxygen was recorded with an online mass spectrometer apparatus (HIDEN QIC-20). Prior to each test, the sample (100 mg) was pre-treated in a purified oxygen stream at 400 °C for 60 min, cooled down to room temperature in oxygen atmosphere and purged by a stream of purified He until stabilization of MS base line. The reactor was heated at the rate of 10 °C/min from 50 to 700 °C. Simultaneously, the desorbed oxygen signal was collected by MS detector.

2.3. Catalytic activity measurement

Catalytic combustion reactions were carried out in a continuous flow micro-reactor constituted of a quartz tube of 4 mm of inner diameter and 400 mm of height at atmospheric pressure. Two hundred milligram catalyst in powdered form (0.2–0.4 mm) was placed at the bed of the microreactor. The feed stream to the reactor was set at 50 cm³ min⁻¹ with the gas hourly space velocity (GHSV) being 15,000 h⁻¹. The feed stream was prepared by delivering liquid *o*-DCB with a syringe pump into dry air, which was metered by a mass flow controller. The injection point was electrically heated to ensure complete evaporation of *o*-DCB. *o*-DCB concentration in reaction feed was set at 1000 ppm. Temperature was measured with a thermocouple located just at the bed thermal point of reactor. Effluent gases were analyzed at a given temperature (to maintain 60 min) on-line by using a GC equipped with FID. The concentrations of Cl_2 and HCl were analyzed by the effluent stream bubbling through a 0.0125 N NaOH solution, and chlorine concentration was then determined by the titration with ferrous ammonium sulphate using N,N-diethyl-p-phenylenedi- amine as an indicator [30]. The concentration of chloride ions in the bubbled solution was determined by using a chloride ion selective electrode [31]. Catalytic activity was measured over the range 170–500 °C and conversion data were calculated by the difference between inlet and outlet CB concentrations.

2.4. *In situ* FTIR studies

In situ diffuse reflectance infrared fourier transform spectroscopy (DRIFTS) experiments were conducted on a Nicolet 6700 FTIR fitted with a nitrogen-cooled mercury–cadmium–telluride detector (MCT). The DRIFTS cell was fitted with CaF_2 windows and a heating chamber that allowed samples to be heated to 800 °C. All the spectra were collected in range of 4000–1200 cm⁻¹ at the resolution of 4 cm⁻¹ and 64 scans. Prior to each infrared experiment, the sample was pretreated with 10% O_2/N_2 at 400 °C for 2 h and then cooled down to 100 °C in order to remove the contaminants. Spectra of the clean catalyst surface were collected and used as the background. Adsorption and reaction were conducted by exposing catalyst samples to a stream of a flowing composed of 1000 ppm

Table 1

Surface and structural property of CoxMny samples.

Samples	Mn/Co (mole) ^a	S_{BET} ($\text{m}^2 \text{ g}^{-1}$) ^b	Crystallite size (nm) ^c	L (nm) ^d	R (nm) ^e	H_2 -TPR ($^{\circ}\text{C}$)	T_{onset}	T_{max}
Co_3O_4	0	29	25	8.082	22.6	200	315	
$\text{Co}_{11}\text{Mn}1$	0.10	88	17	8.090	12.6	225	350	
$\text{Co}_9\text{Mn}1$	0.12	80	13	8.102	8.9	220	335	
$\text{Co}_7\text{Mn}1$	0.13	76	14	8.098	—	215	325	
$\text{Co}_5\text{Mn}1$	0.19	77	14	8.094	10.1	—	—	
$\text{Co}_3\text{Mn}1$	0.35	77	13	8.106	—	—	—	
$\text{Co}_1\text{Mn}1$	0.71	72	12	8.162	11.2	—	—	
$\text{Co}_1\text{Mn}3$	3.50	69	—	—	—	—	—	—
MnO_x	—	5	28	—	—	—	—	—

^a Co/Mn ratios measured by ICP.^b BET surface area.^c The crystallite sizes of spinel particles calculated with the Scherrer equation applied for (3 1 1).^d Lattice parameters.^e The crystallite sizes of spinel particles estimated by TEM.

σ -DCB, 10% O_2 and N_2 balance. *In situ* FTIR spectra were collected from 100 to 380 $^{\circ}\text{C}$ where a steady state was reached.

3. Results and discussion

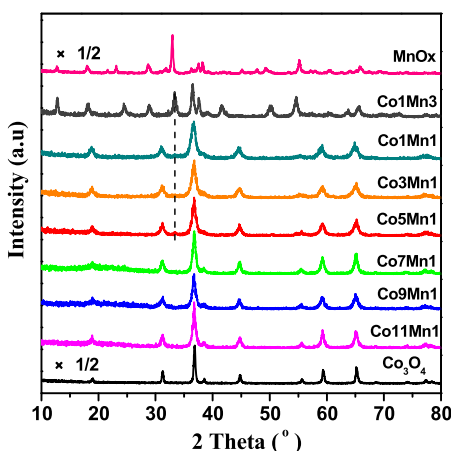
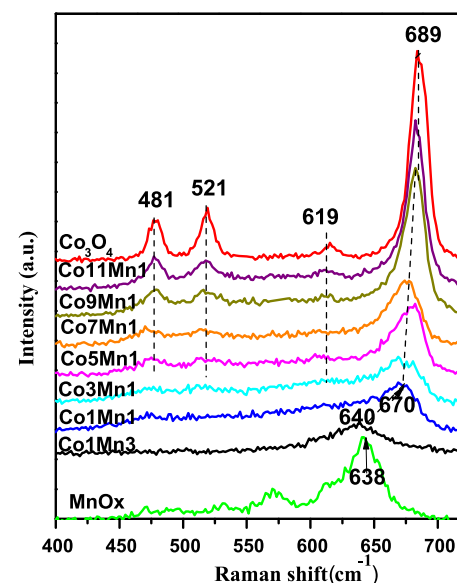
3.1. Characterization of catalysts

3.1.1. XRD

Bulk chemical compositions of as-synthesized catalysts were determined by means of ICP-OES and summarized in Table 1. Co/Mn ratios in CoxMny samples are nearly equal to the nominal value. N_2 adsorption and desorption isotherms (Supporting Information, SI) show that pore size distributions (PSD) of pure Co_3O_4 are in a range of 10–55 nm calculated from the adsorption isotherm branch based on BJH model. With the incorporation of Mn species, pore size becomes small, and PSD, narrow. Pore sizes of $\text{Co}_{11}\text{Mn}1$ and $\text{Co}_9\text{Mn}1$ are concentrated on about 10 and 8 nm, respectively. For $\text{Co}_1\text{Mn}1$, pore size increases to 28 nm with a much broader PSD, implying new structure occurring (see later XRD results). Compared with pure Co_3O_4 ($29 \text{ m}^2 \text{ g}^{-1}$), BET specific surface area of CoxMny samples increases to a large extent (69 – $88 \text{ m}^2 \text{ g}^{-1}$), indicating that the dispersion of CoxMny samples increases. However, pure MnO_x has the lowest surface area, $4.8 \text{ m}^2 \text{ g}^{-1}$, due to its nonporous structure.

Fig. 1 shows wide angle XRD patterns of CoxMny samples. For CoxMny samples with Co/Mn ratio of 1 or higher, eight peaks appear at 19.0, 31.4, 36.9, 38.6, 44.9, 55.7, 59.4 and 65.4 $^{\circ}$, which are ascribed to Co_3O_4 spinel structure (JCPDS no. 74-1656) [28] and

no reflection from CoO is observed. The diffraction peaks of spinel become weaker and broader with Mn amount, suggesting a systematic decrease in the size of spinel particle. Calculation with Scherrer equation applied for (3 1 1) showed that crystalline particle size decreases from 25 nm for pure Co_3O_4 to 12 nm for $\text{Co}_1\text{Mn}1$ (Table 1) and the diffraction peaks shift to smaller 2θ with the increase in lattice parameter from 8.082 to 8.162 \AA , indicating the incorporation of Mn into Co_3O_4 spinel structure. Many studies demonstrated that $\text{Mn}_x\text{Co}_{3-x}\text{O}_4$ solid solution with spinel structure can be prepared by co-precipitation [32–34]. For $\text{Co}_1\text{Mn}3$, several peaks appear at 24.5, 33.5, 36.4, 39.4, 41.6, 50.3, 54.8 and 63.7 $^{\circ}$, characteristic of CoMnO_3 phase (JCPDS #12-0476), and those at 12.8, 18.1, 28.8 and 37.5 $^{\circ}$, of MnO_2 (JCPDS #44-0141). Generally, CoMnO_3 phase can form at 400 $^{\circ}\text{C}$ or lower temperature during preparation of Mn–O–Co binary oxides and transferred into $\text{Mn}_x\text{Co}_{3-x}\text{O}_4$ ($(\text{Co},\text{Mn})(\text{Co},\text{Mn})_2\text{O}_4$) spinel as temperature rises. Since the radius of Co^{2+} (0.78 \AA) and Co^{3+} (0.65 \AA) are closed to those of Mn^{3+} (0.66 \AA) and Mn^{4+} (0.60 \AA), the dissolution of Co ions in MnO_2 lattice is possible [27]. A weak peak appearing at 33.5 $^{\circ}$ over $\text{Co}_5\text{Mn}1$, $\text{Co}_3\text{Mn}1$ and $\text{Co}_1\text{Mn}1$ can be ascribed to CoMnO_3 , indicating that for Mn–O–Co binary oxides with high ratios of Co/Mn, most of CoMnO_3 has transferred into spinel phase. On XRD pattern of pure MnO_x , five strong and sharp peaks appear at 32.9, 38.1, 49.6, 55.2 and 65.8 $^{\circ}$, the

**Fig. 1.** XRD patterns of CoxMny samples with various ratios of Mn/Co.**Fig. 2.** Raman spectra of CoxMny samples with various ratios of Mn/Co.

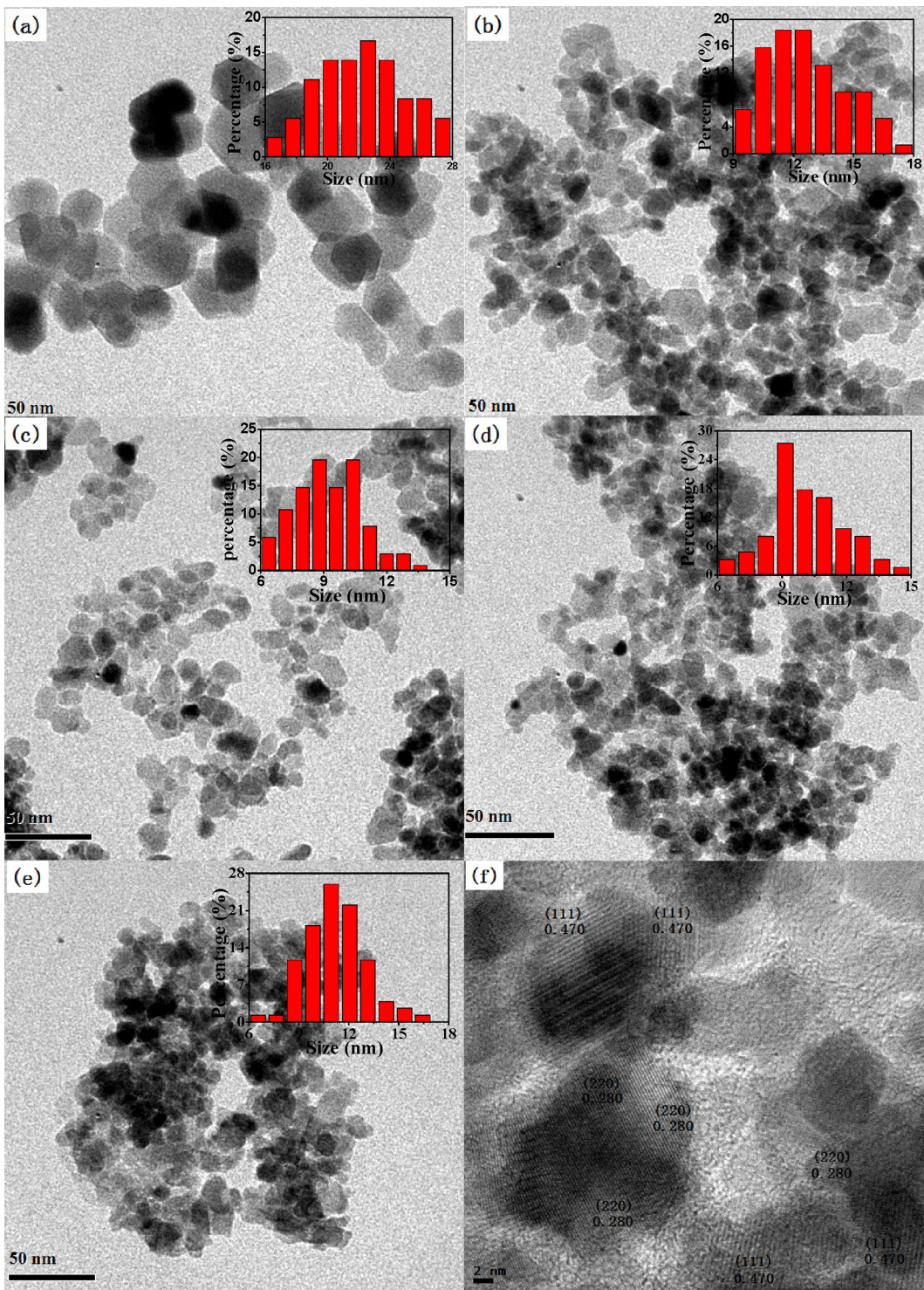


Fig. 3. TEM photos of CoxMny samples with various ratios of Mn/Co and HRTEM, photo of Co_9Mn_1 sample; a— Co_3O_4 , b— $\text{Co}_{11}\text{Mn}_1$, c— Co_9Mn_1 , d— Co_5Mn_1 , e— Co_1Mn_1 and f— Co_9Mn_1 .

indices of incipient $\gamma\text{-Mn}_2\text{O}_3$ crystallization in the form of bixbyite (JCPDS #24-0508), whereas some small peaks can be ascribed to MnO_2 .

3.1.2. Raman

CoxMny samples were investigated by Raman scattering and the resulted spectra are depicted in Fig. 2. Within the range of $400\text{--}800\text{ cm}^{-1}$, pure Co_3O_4 exhibits four expected Raman-active modes: A_{1g} (689 cm^{-1}), F_{2g} (619 and 521 cm^{-1}) and E_g (481 cm^{-1})

[29,35]. The position and width of these bands are consistent well with the reported values for Co_3O_4 spinel [29,35]. A_{1g} (689 cm^{-1}) mode is attributed to the octahedral sites $[\text{CoO}_6]$ in O_{7h} symmetry, whereas F_{2g} (521 cm^{-1}) and E_g (481 cm^{-1}) modes combine the vibration of tetrahedral and octahedral sites [29,36]. Raman bands shift towards lower frequencies and become more asymmetric and broader with Mn amount, which are the consequence of a dopant-induced increase of structural disorder and a decrease in bond strengths (force constants). These results can confirm the

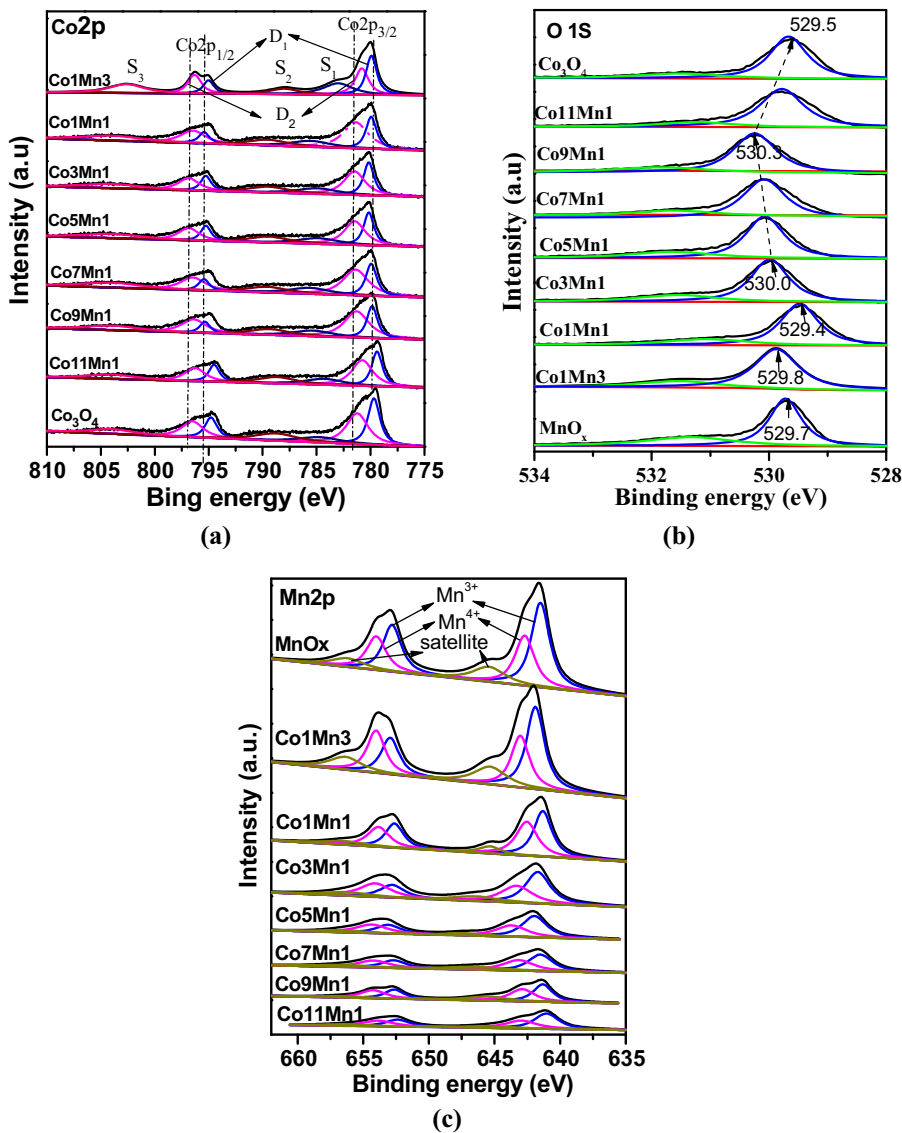


Fig. 4. XPS spectra of Co 2p (a), O 1s (b) and Mn 2p (c) for CoxMny samples with various ratios of Mn/Co.

incorporation of Mn into Co₃O₄ spinel lattice [9,19]. For the samples with Co/Mn ratios of 5 or lower, weak F_{2g} and E_g peaks could not be resolved, due to excessive broadening or appearing CoMnO₃ on the surface. Co1Mn3 presents only one weak band at 640 cm⁻¹, similar to the spectrum of pure MnO_x, on which the band at 638 cm⁻¹ is attributed to a Mn—O—Mn stretching mode ($\nu_{\text{Mn—O—Mn}}$) in Mn₂O₃, indicating that Mn—O—Mn is main structure on the surface of Co1Mn3.

3.1.3. TEM

Fig. 3a–e reveals TEM morphologies of CoxMny samples. Pure Co₃O₄ presents hexagonal prism with an average size of 22 nm. With the incorporation of Mn, nano-particles display amorphous shape and have an average size ranging from 6 to 15 nm, similar to those obtained by Zhang [21]. Compared with the sizes (from 12 to 25 nm) calculated from XRD results, TEM reveals the presence of smaller nano-particles. HRTEM morphology of Co9Mn1 (Fig. 3f) shows cubic lattice with inter-planar distance of 0.285 and 0.470 nm, corresponding to (1 1 0) planes of Co₃O₄ spinel. This is in agreement with the values obtained from X-ray diffraction 0.285 and 0.465 nm. The lattice fringe of crystal phase corresponding to Mn species is not observed, confirming that most of Mn species

of Co9Mn1 enter Co₃O₄ spinel lattice to form Mn_xCo_{3-x}O₄ solid solution [37].

3.1.4. XPS

Fig. 4 shows XPS spectra of Co 2p, Mn 2p and O 1s electronic levels in CoxMny samples. With the procedure similar to that reported by Gautier [38], the spectra of Co in CoxMny catalysts were analyzed on the basis of the fit of the spectrum of Co₃O₄ (Fig. 4a). Thus, all Co2p spectra were deconvoluted into five different contributions (two spin-orbit doublets: Do1 and Do2, and three satellite peaks: Sa1, Sa2 and Sa3) using the following constraints: equal width for the two lines of each doublet, equal width for the two smaller satellite peaks (Sa1 and Sa2), width of the most intense satellite peak (Sa3) fixed to 8.5 eV, and the same constant tail height for all the peaks. D₁ with a binding energy (BE) of 2p level of 779.6–780.1 eV and a 2p_{3/2}–2p_{1/2} splitting of 15.1 eV is characteristic of the octahedral Co³⁺ component of Co₃O₄, and D₂ with BE of 2p level of 780.9–781.4 eV and a 2p_{3/2}–2p_{1/2} splitting of 15.5 eV corresponds to the tetrahedral Co²⁺ [39]. The fitted ratio of Co³⁺/Co²⁺ is observed to be 1.80 (Table 2), lower than the reported value (1.99) [27]. However, as summarized in Table 2, Co³⁺/Co²⁺ ratios for CoxMny samples decrease greatly down to the range of 0.83–0.92,

Table 2
XPS analysis of the fresh CoxMny catalysts.

Samples	Co ³⁺ /Co ²⁺ ^a Co ²⁺ (mol %)	N ^b	Mn ⁴⁺ /Mn ³⁺	O _α /O _β	Mn/Co
Co ₃ O ₄	1.80(2.00) ^c	14.1	–	0.50	0
Co11Mn1	0.89(1.10)	16.8	0.78	0.32	0.17
Co9Mn1	0.86 (1.04)	19.0	0.92	0.33	0.20
Co7Mn1	0.83 (0.90)	17.6	0.85	0.34	0.24
Co5Mn1	0.92(0.79)	17.3	0.89	0.30	0.273
Co3Mn1	0.92(0.36)	14.4	1.06	0.26	0.47
Co1Mn1	0.86(0.04)	10.6	–	0.21	0.97
Co1Mn3	0.93(–)	3.1	0.61	0.28	4.80
MnO _x	–	–	0.53	0.26	–

^a XPS results of the fresh CoxMny catalysts.

^b Co²⁺ concentration.

^c The values calculated according to Mn contents under the assumption that all Mn species substitute for Co³⁺ ions in the octahedral sites and one Mn⁴⁺ ion will produce the additional Co²⁺ ion.

indicating that some Co ions change from Co³⁺ to Co²⁺ as Mn species enter the spinel structure and Co³⁺ is replaced by Co²⁺ and Mn⁴⁺ in octahedral sites [37]. Mn K-edge EXAFS spectra for Mn–Co₃O₄ suggested that Mn atoms primarily occupied octahedral sites in spinel structure [18]. Additionally, from the analyses for crystal structure, magnetic susceptibility, resistivity and electrochemical measurements of Mn_xCo_{3-x}O_x oxides, it can be concluded that Mn³⁺ and Mn⁴⁺ ions could locate in the octahedral sites of spinel structure [40]. According to the assumption that all Mn species substitute for Co³⁺ ions in the octahedral sites and one Mn⁴⁺ ion will produce the additional Co²⁺ ion, Co³⁺/Co²⁺ ratios (the value within brackets in Table 2) calculated from XPS data on compositions of Mn species are close to the ratios obtained directly from Co 2p spectra (SI), indicating that most Mn species should substitute for Co³⁺ ions in the octahedral sites. It is noted that a much lower Co³⁺/Co²⁺ is obtained for Co1Mn1 sample compared with the ratio obtained by direct deconvolution. This difference of Co³⁺/Co²⁺ ratio obtained by two methods is due to the presence of CoMnO₃ in which Co species exist mainly in the form of Co³⁺. For Co1Mn3, the phase structure is composed mainly of CoMnO₃ and MnO₂, and it can be expected that its Co³⁺/Co²⁺ ratio increases.

O 1s spectra of CoxMny samples were deconvoluted into two contributions (Fig. 4b): one with BE of 531.1–531.8 eV is assigned to surface adsorbed oxygen (O_α) [41], and the other with BE of 529.4–530.2 eV, to lattice oxygen (O_β) [42]. O_α/O_β ratio of pure Co₃O₄ is 0.50, whereas O_α/O_β ratio decreases from 0.33 for Co11Mn1 to 0.28 for Co1Mn3 which is similar to the value for MnO_x (0.26). Obviously, Mn species decreases O_α/O_β ratio of CoxMny samples [21]. Because of “Mn ← O” electron-transfer processes, BE of O_β increases with Mn amount and reaches the highest value of 530.3 eV for Co9Mn1 sample (Fig. 4). Most likely, in cubane structure, Mn³⁺/Mn⁴⁺ are binding oxygen very strongly [43]. However, for the samples containing higher Mn amount, BE of O_β decreases gradually (Fig. 5 insert). Considering that Mn⁴⁺ substitution for Co³⁺ at octahedral site will produce another Co²⁺ at octahedral site, Co²⁺ concentration on the surface was correlated to BE of O_β. As shown in Fig. 5, BE of O_β is proportional to Co²⁺ concentration. This phenomenon can be explained by the fact that higher binding energy of Co²⁺ probably changes the coordination environment of lattice oxygen.

The binding energies of Mn 2p_{3/2} and Mn 2p_{1/2} are very similar to those reported in the literature [44,45]. Since the differences between the binding energy values of Mn³⁺ and Mn⁴⁺ ions are small, a peak synthesis procedure, which includes three components – Mn³⁺, Mn⁴⁺, and a satellite [44,45] – was applied. The fitted XPS spectra of Mn 2p are shown in Fig. 4c. The component at 641.2–641.9 eV is attributed to Mn³⁺ and that at 642.7–643.3 eV, to Mn⁴⁺ ions [44]. For pure MnO_x, there exist both Mn³⁺ and

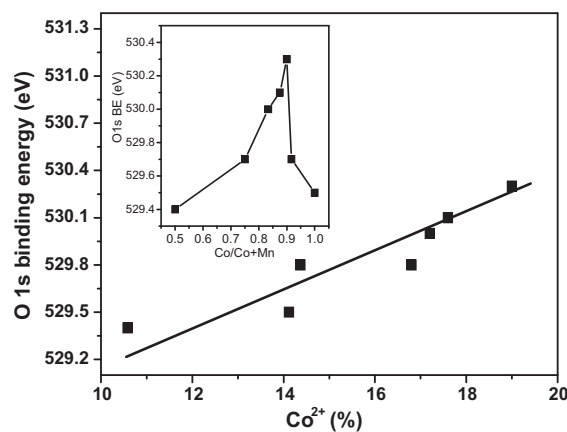


Fig. 5. BE of O 1s 2p level for CoxMny samples with various ratios of Mn/Co.

Mn⁴⁺ species, which is consistent with the presence of Mn₂O₃ and MnO₂ (confirmed by XRD analysis). With incorporation of Mn into spinel lattice, Mn species still are composed of Mn³⁺ and Mn⁴⁺. The value of the Mn⁴⁺/Mn³⁺ ratio (Table 2) in the surface layer of CoxMny samples with well spinel structure such as Co11Mn1, Co9Mn1, Co7Mn1, Co5Mn1 and Co3Mn1 is quite high (0.78–1.06). The ratio of Mn⁴⁺/Mn³⁺ in Co1Mn1 and Co1Mn3 decreases to about 0.51, which is related to the formation of CoMnO₃ phase. Pure MnO_x also presents low ratio of Mn⁴⁺/Mn³⁺ (0.53). Obviously, Co₃O₄ spinel structure is favorable for the transformation of Mn³⁺ ions to Mn⁴⁺ ions. This result is explained by the fact that charge compensation after the substitution of some Co³⁺ ions at octahedral sites with Mn⁴⁺ ions can be achieved by reduction of Co³⁺. Moreover, the enrichment of Mn occurred on the surface of CoxMny samples (Fig. S2), especially for the samples with low Mn amount.

3.1.5. H₂-TPR and O₂-TPD

Fig. 6a and b shows H₂-TPR profiles recorded over CoxMny samples. Pure Co₃O₄ is reduced with two steps [46]: A first peak centered at about 315 °C was associated with the reduction of Co³⁺ ions to Co²⁺ with the concomitantly structural change to CoO, while the second step reduction proceeds within 358–575 °C and attributed to subsequent reduction of CoO to metallic cobalt. A quantitative evaluation of the amounts of hydrogen consumed during reduction was estimated to be 17.0 mmol H₂. As predicted by Co³⁺ → Co²⁺ and Co²⁺ → Co⁰, the ratio between the areas of two peaks was about 1:3. With the incorporation of Mn into Co₃O₄, the first peak shifts to slightly high temperature with the decrease in peak area, which is related to the substitution of Mn⁴⁺/Mn³⁺ for Co³⁺ ions in the octahedral sites. Additionally, the formation of Co–O–Mn in Co₃O₄ spinel structure can make the reducibility of these samples decrease, as pointed previously [43]. For the samples with Co/Mn ratios of 7 or higher, two reduction peaks resemble to the profile of pure Co₃O₄, being ascribed to the stepwise reduction of Mn_xCo_{3-x}O_x solid solution and involving the bulk oxygen species of cobalt and manganese oxides in mixed valences [20]. H₂ consumption at two steps approaches to 1/3, due to a small amount of Mn species added. Three reduction peaks appear at ca. 230, 350 and 450 °C on the profiles of the samples with Co/Mn ratio of 5 or lower. A first weak shoulder peak corresponds to the reduction of Mn₂O₃ to Mn₃O₄ or CoMnO₃ [47], whereas a second broad peak is probably due to the combination of Co³⁺ → Co²⁺ and Mn₂O₃ (MnO₂) → Mn₃O₄. A third peak may correspond to Co²⁺ → Co⁰. It should be noted that new peak is centered at about 597 °C, and its intensity increases with Mn amount. Obviously, this peak is related to the reduction of Mn in Co–O–Mn structure. In fact, two strong broad reduction peaks corresponding to Mn₂O₃

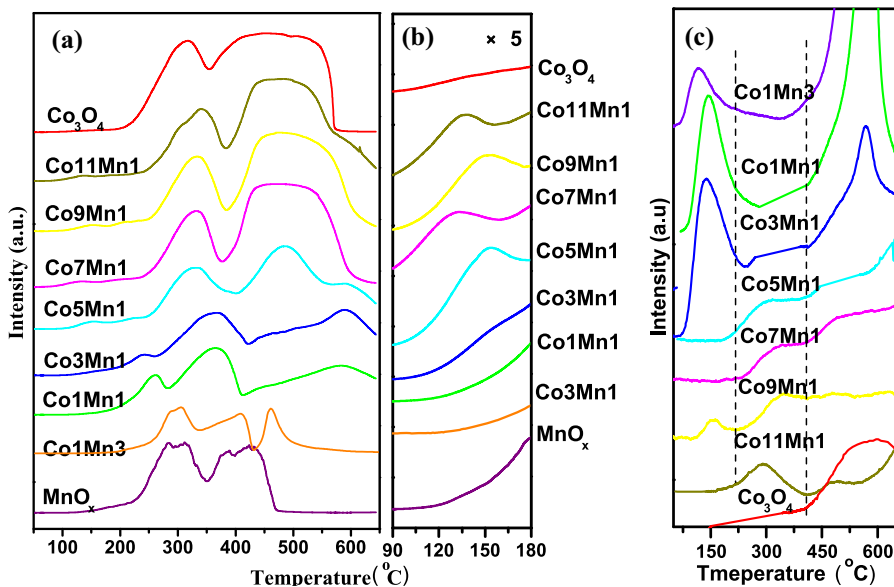


Fig. 6. H_2 -TPR profiles (a and b) and O_2 -TPD (c) of $CoxMny$ samples with various ratios of Mn/Co.

(MnO_2) $\rightarrow Mn_3O_4 \rightarrow MnO$ appear at ca. 285 and 420 $^{\circ}C$ over MnO_x [48,49]. The decrease in reducibility of Mn species in $CoxMny$ samples can be ascribed to strong binding Mn^{3+}/Mn^{4+} in the cubane [43]. In addition, a weak peak at 150 $^{\circ}C$ for $CoxMny$ samples with low Mn amount such as $Co11Mn1$, $Co9Mn1$, $Co7Mn1$ and $Co5Mn1$. This peak can be attributed to very active species on the surface formed during the calcinations in air [50]. As reported, the synthesis of cobalt oxides having a small crystallite size was favorable for the formation of easily reducible sites, which were less abundant on more highly crystalline Co_3O_4 catalysts [51]. And the reduction of O_2 chemisorbed on Co^{2+} ions occurred at lower temperature [52]. In this work, the size of Co_3O_4 particles in $Co11Mn1$, $Co9Mn1$, $Co7Mn1$ and $Co5Mn1$ is much smaller than that of pure Co_3O_4 particles (Table 1), and a significant increase in Co^{2+} is observed (Table 2). Therefore, it could be concluded that this peak is ascribed to the reduction of O_2 chemisorbed on Co^{2+} ions of Co_3O_4 nano-particles with smaller size.

Fig. 6c shows O_2 -TPD profiles recorded over $CoxMny$ samples. O_2 -TPD is an effective method to determine the mobility of oxygen species [53]. Generally, the adsorbed oxygen changes in the following procedures: O_2 (ad) $\rightarrow O_2^-$ (ad) $\rightarrow O^-$ (ad) $\rightarrow O_2^-$ (lattice) [54]. The physically adsorbed oxygen O_2 and chemically adsorbed oxygen O_2^-/O^- species are much easier to desorb than the lattice O_2^- species [55]. The desorption of oxygen at very low temperature (<200 $^{\circ}C$) can be assigned to the physically adsorbed oxygen and/or the ordinarily chemically adsorbed oxygen, while the desorption peaks between 200 and 400 $^{\circ}C$ can be related to the chemically adsorbed oxygen species, and the desorption peak appearing at higher temperatures (>400 $^{\circ}C$) can be attributed to the bulk lattice oxygen. As shown in Fig. 6c, for pure Co_3O_4 , oxygen desorption starts at 150 $^{\circ}C$ and slowly becomes strong, indicating the presence of a small amount of chemically adsorbed oxygen species. However, oxygen desorption increases greatly at 400 $^{\circ}C$ or higher, which may be expected based on bulk thermodynamics. After the introduction of Mn, a distinctive feature is observed: The amount of physically adsorbed oxygen O_2 (100–200 $^{\circ}C$) is different from each other. It is noted that a significant increase in the chemically adsorbed oxygen species desorbed within 200–400 $^{\circ}C$ is observed for $Co11Mn1$, $Co9Mn1$, $Co7Mn1$ and $Co5Mn1$ samples, which is related to higher Co^{2+} concentration in $Co-O-Co$ structure of spinel. As reported, the presence of Co^{2+} species can promote the formation of highly active sites for catalytic oxidation of 1,2-dichloroethane [51] and

CO and C_3H_6 [52]. Here, it can be expected that higher amount of chemically adsorbed oxygen species may significantly contribute to the high activity level for *o*-DCB oxidation in which surface oxygen species participate (see later). Further increase in Mn is unfavorable for evolution activity of chemically adsorbed oxygen species. Most likely, in the cubane structure, Mn^{3+}/Mn^{4+} are binding oxygen too strongly [43]. Indeed, the concentration of Mn species on surface on $Co3Mn1$, $Co1Mn1$ and $Co1Mn3$ samples increase to a large extent. Raising temperature to 400 $^{\circ}C$ or higher, the desorption of lattice O_2^- species become strong and strong, resulted really from the general transition of MnO_x at elevated temperatures through the loss of lattice oxygen [56].

3.2. Catalytic activity

The activity of $CoxMny$ catalysts for decomposition of *o*-DCB is shown in Fig. 7 as a function of temperature. In order to check whether or not some reactions under thermal combustion condition could take place, blank test was carried out by 4 mm crushed quartz glass (20–40 mesh) packed in the reactor. As a result, low conversion is obtained above 350 $^{\circ}C$ and the conversion reaches

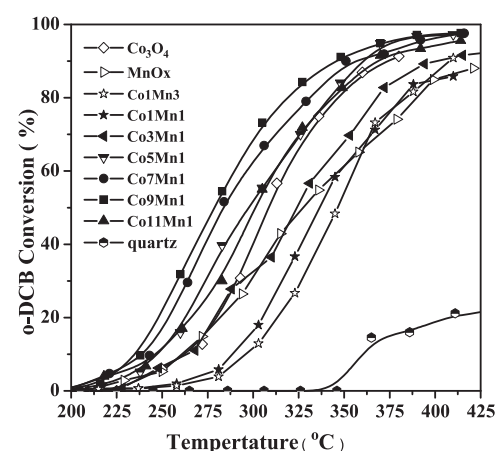


Fig. 7. The conversion curves for *o*-DCB catalytic combustion over $CoxMny$ samples with various ratios of Mn/Co; reaction gas composition: 1000 ppm *o*-DCB, 10% O_2 and N_2 balance; GHSV = 15,000 h^{-1} .

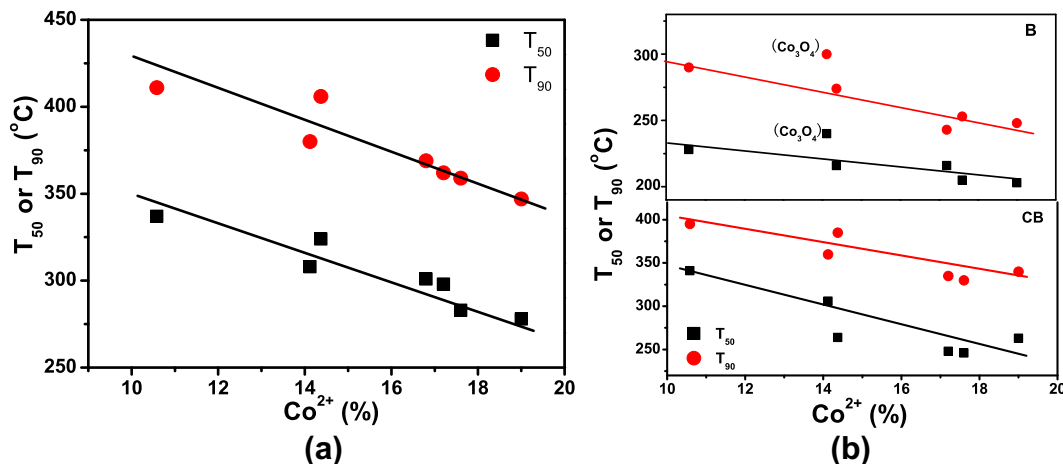


Fig. 8. The effect of Co^{2+} concentration of CoxMny catalysts on T_{50} and T_{90} for o-DCB (a), B and CB (b) catalytic combustion; reaction gas composition: 1000 ppm o-DCB or B or CB, 10% O_2 and N_2 balance; GHSV = 15,000 h^{-1} .

only about 30% even at 453 °C. Pure Co_3O_4 exhibits a considerable activity with T_{50} and T_{90} (the temperature needed for 50% and 90% conversion, respectively) of 298 and 380 °C, respectively. With the incorporation of Mn species, the activity of catalysts is remarkably improved and the conversion curves shift to lower temperature, indicating that the formation of $\text{Mn}_x\text{Co}_{3-x}\text{O}_4$ is favorable for DCB oxidation. Co9Mn1 presents the best activity with T_{90} of about 347 °C, which is closed to T_{90} obtained over $\text{V}_2\text{O}_5/\text{TiO}_2$ -based catalysts [2,4,57]. However, with the increase in Mn content up to $\text{Mn/Co} = 1/5$ or higher, the activity decreases significantly. T_{90} over Co1Mn1 , for example, is 411 °C. It is noted that the activity of MnO_x catalyst at low temperature is similar to that of Co_3O_4 , while the curve section corresponding to higher than 20% conversion shifts to high temperature. As reported previously, MnO_x is susceptible to adsorption of Cl species, while the removal of Cl species was a slow process [7]. Thus, for catalysts containing high Mn amount, such as Co3Mn1 , Co1Mn1 and Co1Mn3 , when the conversion is higher, the concentration of Cl species becomes larger and the reaction becomes retarded. EDS analyses (Table 4) confirmed that Cl deposition on the used catalysts increases with Mn amount. It allows us to further study how the substitute of Mn at octahedral sites influences the activity and stability of CoxMny catalysts.

Fig. 8(a) indicates that T_{50} and T_{90} decrease with the increase in Co^{2+} concentration on the surface, indicating that Co^{2+} is crucial for o-DCB combustion. Co-MOR containing Co^{2+} presented active for o-DCB oxidation [58]. Here, o-DCB molecules could adsorb on Co^{2+} as Lewis acid sites possibly after chlorine abstraction by nucleophilic oxygen [59]. Incorporation with a appreciate amount of Mn increases Co^{2+} concentration and hence promote the adsorption of o-DCB. $\text{Mn}^{3+}/\text{Mn}^{4+}$ and Co^{3+} in CoxMny catalysts should be able

for adsorption of o-DCB. Because Co^{2+} possesses the highest 2p BE, both tetrahedral and octahedral Co^{2+} in the cubane structure can provide optimal binding energy for the intermediate formation on the surface of catalyst. On the other hand, the mobility of oxygen from cubane structure can be reduced in the presence of Mn. The catalysts with containing smaller amount of Mn (a considerable amount of Co–O–Co structure exists) maintain high oxygen mobility and possess high activity for the nucleophilic substitution by O^{2-} ions for the chlorine forming surface intermediates [60]. In other experiment, the activities for benzene (B) and chlorobenzene (CB) oxidation were tested over CoxMny catalysts. As shown in Fig. 8(b), T_{50} and T_{90} decrease with Co^{2+} concentration and follow the order of B < CB < o-DCB, indicating that a similar mechanism can be proposed for B and CB oxidation. o-DCB possesses the lowest reactivity, because the decrease in electron density of ring will influence the adsorption of o-DCB on Co^{2+} in the cubane structure.

Considering the effect of surface area, the specific rates at 250 °C was calculated based on mole of o-DCB transformed per minute and per surface area (Table 3). Clearly, the rate increases with Co^{2+} concentration (Fig. 4S). Taking the concentration of O_2 and o-DCB having no significant change within 20% conversion, the temperature dependence of the reaction rate can be used to generate apparent activation energies. The associated E_a values with 95% confidence limits of o-DCB conversion over Co_3O_4 , Co11Mn1 and Co9Mn1 are 90.4, 89.9 and 88.6 kJ mol^{-1} within the experimental temperature range (Table 3) and slightly higher than the E_a value obtained over $\text{V}_2\text{O}_5/\text{TiO}_2$ (82 kJ mol^{-1}) [61]. The similarity in E_a indicates that the difference in the rate at 250 °C can be ascribed to the difference in Co^{2+} concentration. Co9Mn1 with the largest number of Co^{2+} sites presents the largest rate of 0.033 $\mu\text{mol}/\text{m}^2 \text{ min}$.

Table 3
The activity of CoxMny catalysts with various ratios of Co/Mn.

Samples	o-DCB				B		CB	
	T_{50} (°C)	T_{90} (°C)	Rate ^a ($\mu\text{mol}/\text{m}^2 \text{ min}$)	E_a KJ/mol	T_{50} (°C)	T_{90} (°C)	T_{50} (°C)	T_{90} (°C)
Co_3O_4	308	380	0.023	90.4	240	300	305	358
Co11Mn1	301	369	0.030	89.9	207	250	258	353
Co9Mn1	278	347	0.033	88.6	203	248	263	340
Co7Mn1	283	359	0.020	97.1	205	253	246	330
Co5Mn1	298	362	0.017	122.1	216	243	248	335
Co3Mn1	324	406	0.010	126.0	216	274	254	386
Co1Mn1	337	411	0.003	126.4	228	290	341	393
Co1Mn3	345	<450	0.022	120.2	223	290	339	386
MnO_x	328	<450	0.129	–	222	281	305	379

^a The specific rates, calculated based on the mole of o-DCB transformed per minute and per surface area according to the conversion at 250 °C showed in Fig. 7.

Table 4Textural, structural and chlorine content of the used CoxMny catalysts^a.

Samples	S_{BET} ($\text{m}^2 \text{g}^{-1}$)	Crystallite size (nm) ^b	$\text{Co}^{3+}/\text{Co}^{2+}$	Mn/Co	$\text{Mn}^{4+}/\text{Mn}^{3+}$	Cl ^c (wt%)
Co_3O_4	28	27	1.20 (1.20) ^d	0	–	0.88 (2.0.1) ^d
Co11Mn1	87	16	0.99	0.17	0.90	2.25
Co9Mn1	81	13	0.97 (0.96)	0.19	0.85(0.84) ^d	2.61 (2.88)
Co7Mn1	82	12	0.96	0.25	0.83	3.48
Co5Mn1	85	10	0.95	0.30	0.67	3.18
Co3Mn1	83	8	0.97	0.47	0.63	3.51
Co1Mn1	79	9	0.98	1.04	0.59	3.58
MnO_x	4	34	–	–	–	2.22

^a The catalysts used for 8 h under reaction condition as described in Fig. 11(a).^b The crystallite sizes of spinel particles calculated with the Scherrer equation applied for (311).^c Cl (wt%) on the used CoxMny catalysts determined by EDS.^d The values obtained by XPS for the used catalysts for 35 h under reaction condition as described in Fig. 11(b).

However, a further increase in Mn can change oxygen mobility of catalysts so that high rate can be obtained over Co3Mn1, Co1Mn1 and Co1Mn3 only at higher temperature. Co5Mn1 with a suitable Co^{2+} concentration possesses intermediate oxygen mobility and so Ea increases to some extent. It should be noted that the rate over Co_3O_4 sample with smaller Co^{2+} concentration is higher. This result can be explained by high efficiency factor of catalysts with lower surface area.

3.3. Analyses of products

The analyses for effluent gas show that reaction products are composed mainly of CO_x (99.5% carbon balance), H_2O , HCl and Cl_2 . Other containing-carbon byproducts are B, CB and 1,2,4-TCB (TCB)

whose distributions during the conversion of *o*-DCB are shown in Fig. 9. The amount of B and CB in the effluent is below 40 ppm within the range of reaction temperature (Fig. 9a and b). The formation of B and CB involves in the break of C–Cl bonds of DCB. Considering the fact that the conversions of B and CB reach completion at 300 and 400 °C over CoxMny catalysts, most of B and CB can be converted quickly if formed. Thus, it is reasonable to deduce that the decomposition of π -complex of *o*-DCB with active sites (Co^{2+}) is probably carried out through the attack of oxygen species. Here, C–Cl bonds of *o*-DCB can be broken with one or two steps. TCB concentration is found to be 2–22 ppm over CoxMny catalysts (Fig. 9c). For pure Co_3O_4 , TCB is initially formed at 175 °C and reaches 22 ppm as maximum at 315 °C with 4% selectivity. At 90% conversion, 12 ppm TCB is still observed (Fig. 9c). With the increase in Mn content, the

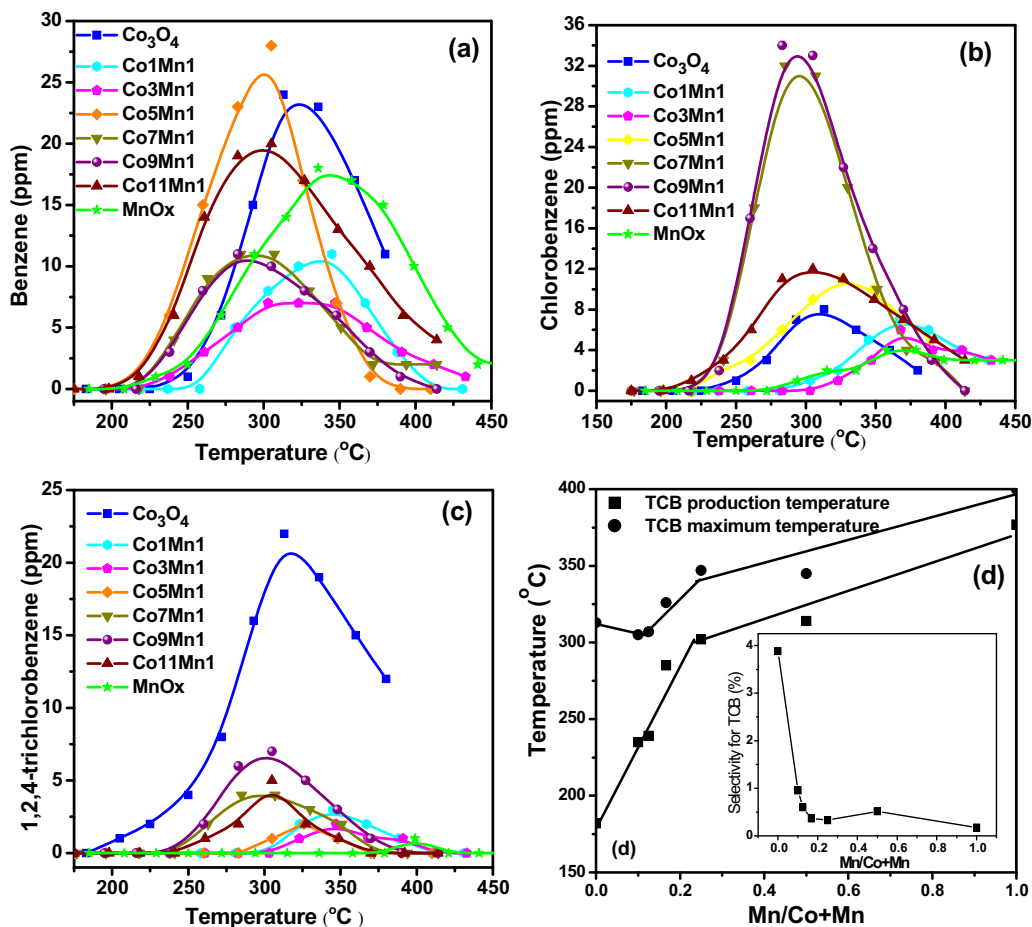


Fig. 9. The distribution of products for *o*-DCB catalytic combustion over CoxMny samples with various ratios of Mn/Co; a-B, b-CB, c-TCB and d-temperature for initial formation of TCB and TCB selectivity; reaction gas composition: 1000 ppm *o*-DCB, 10% O_2 and N_2 balance; GHSV = 15,000 h^{-1} .

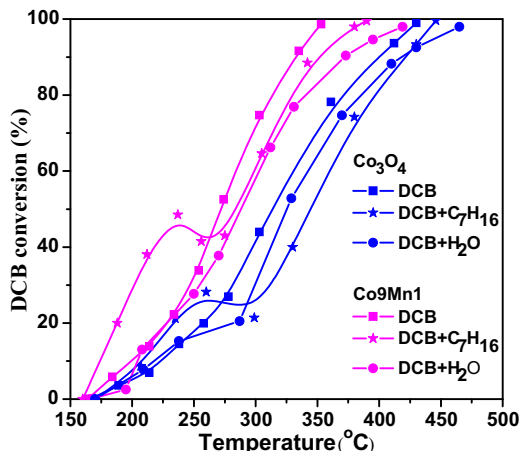


Fig. 10. The effect of water and heptane on *o*-DCB catalytic combustion over Co_3O_4 and Co_9Mn_1 ; DCB alone: DCB 1000 ppm; DCB + water: DCB 1000 ppm + 3% (V/V) water; DCB + C_7H_{16} : DCB 500 ppm + C_7H_{16} 500 ppm; in all cases, 10% O_2 and N_2 balance; $\text{GHSV} = 15,000 \text{ h}^{-1}$.

distribution curves of TCB shift to higher temperature and the maxima of TCB decrease from 7 ppm for Co_9Mn_1 to 2 ppm for Co_3Mn_1 with the drop of selectivity to 0.5% (Fig. 9d). For all Co_xMn_y catalysts, TCB is not detected until 250 °C and almost disappear when the conversion approaches completion. Over MnO_x , only 1 ppm of TCB was detected at 400 °C. Obviously, the incorporation of Mn effectively inhibits the activity of Co_3O_4 for chlorination of *o*-DCB. According to the fact that Cl_2 occurs initially at 300 °C for all catalysts under study (SI), it can be concluded that TCB is produced through the reaction of adsorbed Cl species with *o*-DCB. XPS analyses for the used catalysts showed that BE of Cl 2p over Co_9Mn_1 is 198.6 eV, higher than that of Co_3O_4 , 198.2 eV (SI), indicating that the strength of Cl adsorption was modified by Mn. Low activity for chlorination of *o*-DCB over Co_xMn_y is related likely to the increase in BE of Cl 2p.

3.4. The effect of water or heptane

It is necessary to investigate the effect of water on the activity of catalysts for *o*-DCB combustion. *o*-DCB conversion over Co_3O_4 and Co_9Mn_1 at space velocity of 15,000 h^{-1} as a function of temperatures was obtained as reaction proceeded in the presence of 3% (V/V) water (Fig. 10). In the presence of water, T_{90} over Co_9Mn_1 and Co_3O_4 catalysts are classified as 373 °C and 423 °C, respectively, which increase to a significant extent compared with the data without water in Table 3 (347 °C and 380 °C). As known, the adsorbed H_2O can be dissociated into H^+ and OH^- on metal oxides, and hydroxyl groups will compete with *o*-DCB or oxygen for active sites and thus inhibit the reaction. On the other hand, the strength of hydroxyl adsorption may be higher than that of Cl species in many cases. Here, no TCB is detected within FID or ECD detection limit, indicating that the chlorination of *o*-DCB with the adsorbed Cl species is inhibited probably through the removal of Cl species with water. The effect of water on the oxidation of chlorinated aromatics has also been studied on some other occasions. Amiridis found that water promoted the reaction at low temperature through the removal of Cl species and C species on the surface, but it inhibited at high temperature the oxidation of dichlorobenzene over $\text{V}_2\text{O}_5/\text{TiO}_2$ catalysts due to the adsorption of water on the active sites [62]. Bertinchamps et al. observed that the addition of water decreased the number of strong Brønsted acid sites involved in the adsorption of chlorobenzene [63].

Van den Brink reported that hydrocarbon could remove Cl species from the surface of Pt catalysts [64,65]. In this work, the

effects of feeding heptane into the reaction mixture on the activity of Co_9Mn_1 and Co_3O_4 were investigated (Fig. 10). At low temperature the conversion of *o*-DCB in binary mixture really was promoted, and the temperature for 10% conversion decreases by 16–25 °C. This improvement may involve an H-atom abstraction from heptane on catalysts, which is reactive for the combination with the adsorbed Cl species to form HCl . Van den Brink described this process in catalytic combustion of CB on $\text{Pt}/\text{Al}_2\text{O}_3$ [64]. However, raising temperature, the decrease in activity is observed, and T_{90} shifts to higher temperature, indicating that the consumption of surface oxygen in heptane oxidation decreases oxygen species. No TCB is detected over these two catalysts with the presence of heptane, indicating that the adsorption of Cl species is retarded greatly. So, the removal of the strongly adsorbed Cl species produced during the decomposition of *o*-DCB can be promoted by hydrogen species from the hydrocarbon.

3.5. Catalyst stability and characterisation of used samples

Catalyst stability tests were carried out by feeding the stream containing 1000 ppm *o*-DCB and 10% O_2 at 300 °C at space velocity 15,000 h^{-1} (Fig. 11a). Within first 60 min, the conversion over pure MnO_x decreases from 30 to 15%, and after that keep stable for 7 h. The catalysts with higher Mn content such as Co_1Mn_3 , Co_1Mn_1 and Co_3Mn_1 present a similar tendency and the conversion decreases to 14, 14 and 30% within first few minutes, respectively. It was generally thought that the accumulation of Cl species on MnO_x based catalysts can result in the deactivation of catalysts. EDS analyses (Table 4) confirm that Cl deposition on the used catalysts increased with Mn content. As known, adsorbed Cl species can be removed through Deacon reaction ($2\text{HCl} + \text{O}_2 \rightarrow \text{Cl}_2 + \text{H}_2\text{O}$) or chlorination of reactants. Therefore, the decrease in activity of these catalysts is related to poor activity for *o*-DCB chlorination and Deacon reaction. For these catalysts with poor stability, strong Cl adsorption made $\text{Mn}^{4+}/\text{Mn}^{3+}$ ratio decrease to a significant extent, while other properties, such as crystallite size, surface area, pore structure, element distribution on surface and $\text{Co}^{3+}/\text{Co}^{2+}$ ratio, have no modifications (Table 4). On Mn based catalysts, there is a temperature for obtaining stable activity of CB catalytic combustion, which was generally higher than 350 °C [7,66]. Liu considered that oxy-chlorinated manganese (MnO_yCl_z) can be formed at high temperature [67] which was stable active species for CB catalytic combustion. Over Co_3O_4 , Co_1Mn_1 , Co_9Mn_1 , Co_7Mn_1 and Co_5Mn_1 , the conversion increases slightly within first 100 min and then maintains stable at 55%, 70%, 71%, 68% and 59% for 8 h. Main products in effluent are HCl , CO_x and H_2O and trace TCB. The selectivity for TCB increases with reaction time (Fig. 11c), suggesting that Cl species deposited on catalyst surface increases with time at the same conversion. Characterization for these used catalysts shows that neither change in structure of bulk and surface nor oxidation state of elements in catalysts is observed (Table 4). However, the deposition of Cl species, increases with Mn amount (Table 4). Obviously, high stability for catalysts with high Co/Mn ratio is related to *o*-DCB chlorination. Beatriz found that Co_3O_4 showed a good ability to resist chloride poisoning and stable activity for the catalytic combustion of dichloroethane at 250 °C for 140 h was observed [68]. As reported previously, bonding energies of V–O and V–Cl were 121 kJ/mol [69], while those of Co–O and Co–Cl were 159 kJ/mol and 117 kJ/mol, respectively [70]. No deactivation of $\text{V}_2\text{O}_5/\text{TiO}_2$ -based catalysts was observed during combustion of CVOC, probably due to easy removal of Cl species at V sites. High stability of Co based catalysts for *o*-DCB combustion can be ascribed to lower bonding energies of Co–Cl.

In another test, the stabilities of Co_9Mn_1 and Co_3O_4 at 3000 ppm *o*-DCB at 370 °C were investigated (Fig. 11b). Within first 5 h, there is an obvious initiation within which the conversion increases from 0% to 40% and 60% over Co_3O_4 and Co_9Mn_1 , respectively. After

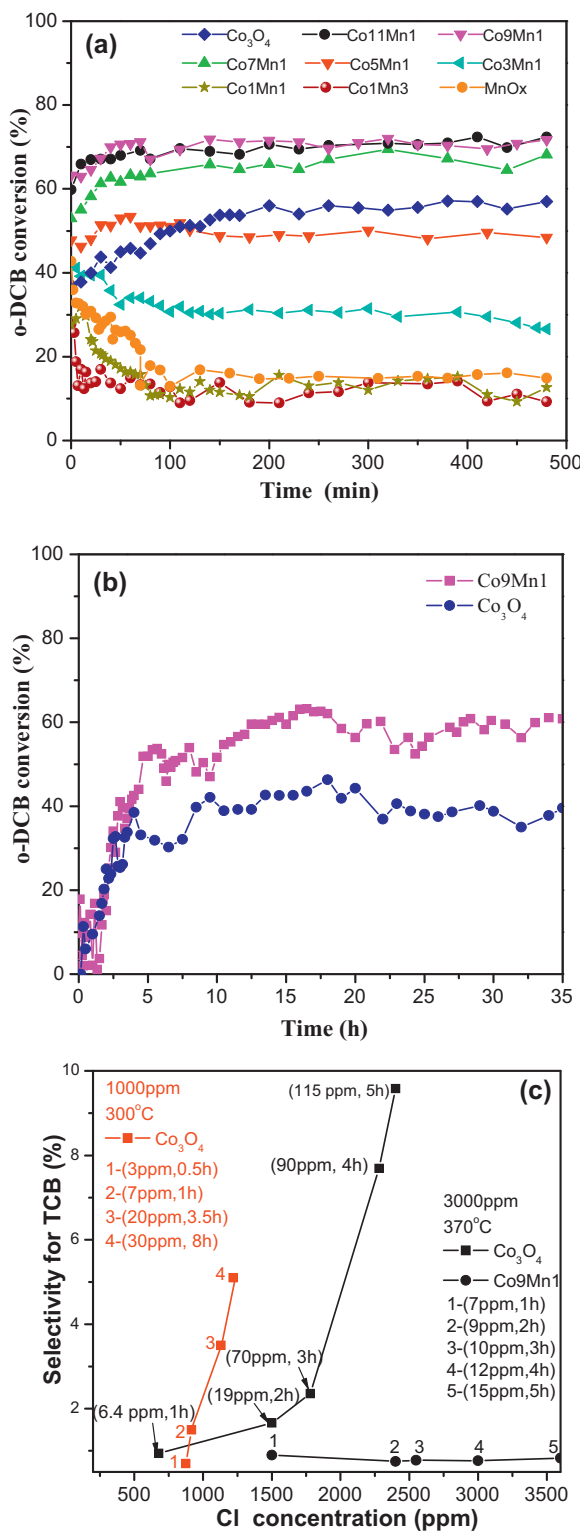


Fig. 11. The activity for o-DCB catalytic combustion on stream feed; a-1000 ppm o-DCB and 10% O₂; b-3000 ppm o-DCB and 10% O₂; GHSV = 15,000 h⁻¹; c-selectivity for TCB at different concentration of Cl species produced.

that, both catalysts show stable activity for 35 h. TCB selectivity over Co₃O₄ increases with Cl species produced and reaches 10% at 35 h (Fig. 11c), which is higher than that obtained at 300 °C at 1000 ppm o-DCB (4%), indicating that raising either temperature or concentration of Cl species produced is favorable for chlorination. However, under the same condition, only 0.3% selectivity for

TCB is obtained over Co₉Mn₁ (Fig. 11c), which may be ascribed to high activity for TCB oxidation and poor activity for chlorination at 370 °C. XPS analyses showed 2.01 and 2.88% Cl deposited on the surfaces of Co₃O₄ and Co₉Mn₁ after reaction, respectively. As known, oxy-chlorinated metals were considered to be active for dissociation of C–Cl. In the presence of 3% (V/V) H₂O, the activity initiation of Co₃O₄ and Co₉Mn₁ is also observed and the curves of conversion *via* time are similar to those without H₂O. Inorganic Cl species on the above used Co₉Mn₁ and Co₃O₄ catalysts in the presence of H₂O decrease greatly (determination by XPS), and the corresponding TCB selectivity almost decreases to zero. It can be concluded that the increase in conversion within initiation could not be ascribed to the formation of oxy-chlorinated metals, and the production of TCB is related to Cl species adsorbed. Characterization for Co₃O₄ and Co₉Mn₁ used at 370 °C for 35 h shows that operation over a prolonged time did not lead to a larger change in oxidation state (Table 4).

3.6. *In situ* FTIR studies

FTIR spectra collected at different temperature during the treatment of Co₉Mn₁ with the reaction feed containing 1000 ppm o-DCB and 10% O₂ for 1 h are shown in Fig. 12a. The bands at 1578, 1458, and 1435 cm⁻¹ can be assigned to the C=C degenerate stretching vibrations of the aromatic ring [71]. The bands at 1578 and 1458 cm⁻¹ were shifted slightly from the 1588 and 1461 cm⁻¹ positions seen for gas-phase o-DCB (not shown). In a similar example of chlorobenzene adsorption on TiO₂ [60], the gas-phase band at 1588 cm⁻¹ was shifted to 1582 cm⁻¹ after, an effect attributed to the formation of a π-complex between surface Ti⁴⁺ ions and the aromatic ring. It was further proposed that such a complex was formed on a dehydroxylated surface, while a dual-site interaction (i.e., OH· · · π-electron and OH· · · Cl) occurred on surfaces with high hydroxyl group concentrations [72]. A similar mechanism can be proposed for o-DCB adsorption on Co₉Mn₁ sample. The intensities of three bands at 1578, 1458, and 1435 cm⁻¹ decrease with the decrease in temperature from 100 to 330 °C, indicating that the corresponding adsorption species are oxidized gradually. The bands at 1332–1344 cm⁻¹ can be assigned to partially oxidized surface species (i.e., formates, acetates and maleates) [72]; the bands at 1454 and 1532 cm⁻¹, to carboxylates of acetate type [60,73]; the bands at 1400 and 1560 cm⁻¹, to carbonate bidentate (Fig. 8a trace c and d) [72], which are not observed until 285 °C where the conversion of o-DCB approaches 56% (Fig. 7) and moreover, their intensities increase with temperature, suggesting that the species characterized with bands at 1578, 1458, and 1435 cm⁻¹ could be a reactive intermediate. The band appearing at 1448 cm⁻¹ at 330 °C (Fig. 12 a trace d) is ascribed to chlorobenzene [72]. Weak bands at 1616, 1254, 1566, and 1410 cm⁻¹ (Fig. 12a trace c and d), as reported [72], can be assigned to chlorinated surface acetates and/or acetyl halides, such as CH₃COCl⁻ or CH₂ClCOO⁻ [61]. The formation of different intermediates containing oxygen could be related to different active oxygen species. Oxygen molecules from gas phase can adsorb on different active sites, such as Co₃O₄ and Mn_xCo_{3-x}O₄ nano-particles, to produce different active oxygen species which will attack carbon bonded to Cl with bond-breaking of aromatic ring. Shoulders at 1616 and 1636 cm⁻¹ increase with temperature, due to the formation of water resulted from oxidations. These results are different from that obtained in many case where the bands at 1247–1285 cm⁻¹ and at 1688 cm⁻¹ assigned to the C–O stretching vibrations of phenolate or catecholate-type species and the C=O stretching vibrations of quinones species formed after nucleophilic substitution on different sites can be observed [6,60,73]. It is reasonable to deduced that surface oxygen formed through dissociation of oxygen on active sites is highly active, and the phenolate or catecholate-type species and quinones species can be

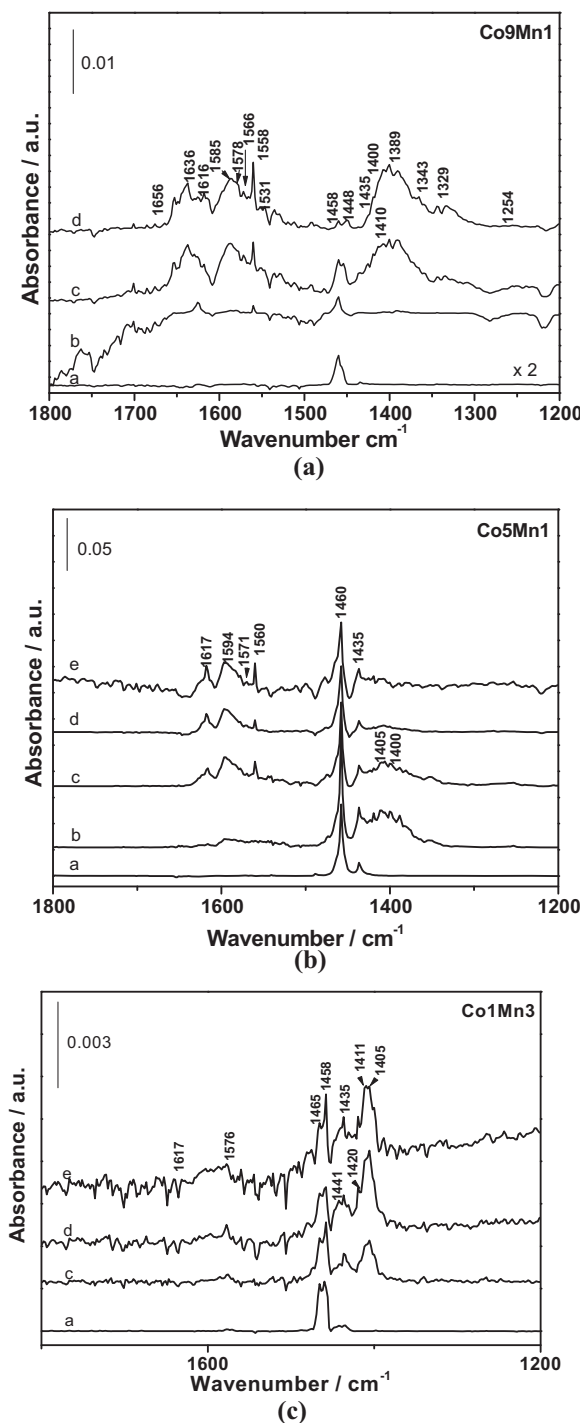


Fig. 12. *In situ* FTIR spectra of Co9Mn1, Co5Mn1 and Co1Mn3 catalysts collected at (a) 100 °C, (b) 220 °C, (c) 285 °C, (d) 330 °C and (e) 380 °C in a stream of 1000 ppm *o*-DCB, 10% O₂ and N₂ for 1 h.

oxidized quickly further into the above mentioned partially oxidized surface species if produced.

Under reaction condition, the spectra of Co5Mn1 (Fig. 12b) included bands similar to those seen for *o*-DCB adsorption and oxidation. It should be pointed out that the bands at 1332–1344 cm⁻¹ and 1532 cm⁻¹, assigned to formates, acetates, and maleates, disappear at 330 °C, while the bands at 1400 and 1560 cm⁻¹, to carbonate bidentate, become weak with raising temperature (Fig. 12b trace b and c). These phenomena indicate that with the increase in Mn content in Co₂O₃ spinel structure from 10% to 17%, the partially

oxidized surface species are formed difficultly or they become not stable.

For Co1Mn3 catalyst, the bands at 1458, and 1435 cm⁻¹ for *o*-DCB adsorption clearly split into two bands at 1465 and 1458 cm⁻¹, and 1441 and 1435 cm⁻¹, respectively. This split could suggest *o*-DCB adsorption on two different types of sites associated with CoMnO₃ and MnO₂ (Fig. 12c). For the same reason, the band at 1400 cm⁻¹, assigned to carbonate, split into two bands at 1411 and 1405 cm⁻¹. Except for the band of carbonate, all of the bands assigned to partially oxidized surface species within the experimental range of temperature are not observed. Actually, the oxidation of *o*-DCB over Co1Mn3 occurs to a significant extent at 285 °C after (with conversion of 6%, Fig. 7) and the carbonate is formed on the surface (Fig. 12c trace c). Here, partially oxidized surface species could be not stable under the attack by lattice oxygen species or active surface oxygen either from CoMnO₃ or MnO₂ and quickly converted into CO_x and H₂O.

In order to obtain deep insights into this reaction, a mechanism over Co9Mn1 consisting of five elementary steps is schematized: (1) absorption of *o*-DCB on Co²⁺ as Lewis acid sites to form a π -complex; (2) chlorine abstraction by nucleophilic oxygen from Co₃O₄ nano-particles or Co–O–Co species; (3) adsorption of the gas-phase oxygen on the surface to replenish the consumed oxygen; (4) the formation of partially oxidized surface species such as formates, acetates, maleates and carboxylates of the acetate type, (5) the complete oxidation to CO₂, H₂O, HCl and Cl₂. Obviously, Co²⁺ sites nearing to Co₃O₄ nano-particles or Co–O–Co species are critical for *o*-DCB combustion. In particular, oxygen mobility becomes dominant for *o*-DCB combustion. The amount of Mn species added need be small in order to maintain the existence Co–O–Co species where oxygen mobility is high. The substitute of Mn species for Co³⁺ at octahedral sites in Co₃O₄ spinel structure with small amount promotes the dispersion of Co₃O₄ as well as Co²⁺ concentration, and thus improves the activity for *o*-DCB combustion. At the same time, Mn modifies the strength of Cl adsorption on Co species, which results in great decrease in activity for *o*-DCB chlorination.

4. Conclusion

CoxMny catalysts with different Co/Mn ratios were prepared by co-precipitation. XRD and Raman analyses show the incorporation of Mn into Co₃O₄ spinel structure greatly increases the dispersion of spinel. The substitute of Mn species for Co³⁺ at octahedral sites in Co₃O₄ spinel structure with small amount can increase Co²⁺ concentration which is correlated to the binding energy of surface lattice oxygen. The oxygen mobility of surface active oxygen is retarded by Mn species. The activity for *o*-DCB oxidation of Mn_xCo_{3-x}O₄ catalysts increases with Co²⁺ concentration. Co9Mn1 with the highest Co²⁺ concentration and available Co–O–Co species presents the highest activity with T₉₀ of 347 °C. Moreover, Mn species can retard greatly the formation of 1,2,4-TCB. CoxMny catalysts with the Co/Mn = 5 or higher present high stability during *o*-DCB oxidation, especially Co9Mn1 which maintains high stability at least for 35 h at 3000 ppm *o*-DCB and 10% O₂ and at GHSV = 15,000 h⁻¹. *In situ* FTIR studies reveal possible reaction pathway: *o*-DCB adsorbs at active sites through the formation of π -complex with ring, and active oxygen attacks adsorption intermediate to form formates, acetates, maleates; carboxylates of the acetate type, and finally CO₂ and H₂O.

Acknowledgments

This research was supported by Development Program for National Natural Science Foundation of China (Nos. 21277047, 21477036 and 21307033), Commission of Science and Technology

of Shanghai Municipality (No. 11JC1402900), and the Opening Project of Key Laboratory of Nuclear Radiation and Nuclear Energy Technology, Chinese Academy of Sciences (NRNE-OP2012001).

Appendix A. Supplementary data

Supplementary data associated with this article can be found, in the online version, at <http://dx.doi.org/10.1016/j.apcatb.2014.10.047>.

References

- [1] M. Taralunga, B. Innocent, J. Mijoin, P. Magnoux, *Appl. Catal. B: Environ.* 75 (2007) 139–146.
- [2] S.D. Krishnamoorthy, J.P. Baker, M.D. Amiridis, *Catal. Today* 40 (1998) 39–46.
- [3] B.H. Aristizábal, C. Maya, C.M.D. Correa, *Appl. Catal. A: Gen.* 335 (2008) 211–219.
- [4] J.S. Choi, C.B. Shin, T.J. Park, D.J. Suh, *Appl. Catal. A: Gen.* 311 (2006) 105–111.
- [5] K. Poplawski, J. Lichtenberger, F.J. Keil, K. Schnitzlein, M.D. Amiridis, *Catal. Today* 62 (2000) 329–336.
- [6] B.H. Aristizábal, C.M.D. Correa, A.I. Serykh, C.E. Hetrick, M.D. Amiridis, *J. Catal.* 258 (2008) 95–102.
- [7] X.Y. Wang, Q. Kang, D. Li, *Appl. Catal. B: Environ.* 86 (2009) 166–175.
- [8] X.D. Ma, Q. Sun, X. Feng, X. He, J. Guo, H.W. Sun, H.Q. Cao, *Appl. Catal. A: Gen.* 450 (2013) 143–151.
- [9] D.A. Aguilera, A. Perez, R. Molina, S. Moreno, *Appl. Catal. B: Environ.* 104 (2011) 144–150.
- [10] J.I. Gutiérrez-Ortiz, R. López-Fonseca, U. Aurrekoetxea, J.R. González-Velasco, *J. Catal.* 218 (2003) 148–154.
- [11] R. López-Fonseca, B. de Rivas, J.I. Gutiérrez-Ortiz, A. Aranzabal, J.R. González-Velasco, *Appl. Catal. B: Environ.* 41 (2003) 31–42.
- [12] W. Zhao, J. Cheng, L. Wang, J.L. Chu, J. k. Qu, Y.H. Liu, S.H. Li, H. Zhang, J.C. Wang, Z.P. Hao, T. Qi, *Appl. Catal. B: Environ.* 127 (2012) 246–254.
- [13] S.K. Agarwal, J.J. Spivey, J.B. Butt, *Appl. Catal. A: Gen.* 81 (1992) 239–255.
- [14] X.D. Ma, J.S. Shen, W.Y. Pu, H.W. Sun, Q. Pang, J. Guo, T. Zhou, H.Q. Cao, *Appl. Catal. A: Gen.* 466 (2013) 68–76.
- [15] J.S. Choi, H.K. Youn, B.H. Kwak, Q. Wang, K.S. Yang, J.S. Chung, *Appl. Catal. B: Environ.* 91 (2009) 210–216.
- [16] S. Rajaram, P.B. Armstrong, B.J. Kim, Jean M.J. Fréchet, *Chem. Mater.* 21 (2009) 1939–1947.
- [17] B. Meng, Z.B. Zhao, X.Z. Wang, J.J. Liang, J.S. Qiu, *Appl. Catal. B: Environ.* 129 (2013) 491–500.
- [18] J. Rosen, G.S. Hutchings, F. Jiao, *J. Catal.* 310 (2014) 2–9.
- [19] N. Bahlawane, P.H.T. Ngamou, V. Vannier, T. Kottke, J. Heberle, K. Kohse-Höinghaus, *Phys. Chem. Chem. Phys.* 11 (2009) 9224–9232.
- [20] C. Shi, Y. Wang, A.M. Zhu, B.B. Chen, C.T. Au, *Catal. Commun.* 28 (2012) 18–22.
- [21] Q.H. Zhang, X.H. Liu, W.Q. Fan, Y. Wang, *Appl. Catal. B: Environ.* 102 (2011) 207–214.
- [22] Y.Z. Feng, X.L. Zheng, *ChemCatChem* 4 (2012) 1551–1554.
- [23] F. Rubio-Marcos, V. Calvino-Casilda, M.A. Banares, J.F. Fernandez, *ChemCatChem* 5 (2013) 1431–1440.
- [24] L. Yan, T. Ren, X.L. Wang, D.Ji, J.H. Suo, *Appl. Catal. B: Environ.* 45 (2003) 85–90.
- [25] Z.K. Zhao, X.L. Lin, R.H. Jin, G.R. Wang, T.H. Muhammad, *Appl. Catal. B: Environ.* 115–116 (2012) 53–62.
- [26] Y. Lou, L. Wang, Y.H. Zhang, Z.Y. Zhao, Z.G. Zhang, G.Z. Lu, Y. Guo, *Catal. Today* 175 (2011) 610–614.
- [27] S. Todorova, H. Kolev, J.P. Holgado, G. Kadinov, C. Bonev, R. Pereñíguez, A. Caballero, *Appl. Catal. B: Environ.* 94 (2010) 46–54.
- [28] J.H. Li, X. Liang, S.C. Xu, J. Hao, *Appl. Catal. B: Environ.* 90 (2009) 307–312.
- [29] W.B. Li, Y. Lin, Y. Zhang, *Catal. Today* 83 (2003) 239–245.
- [30] J.R. González-Velasco, A. Aranzabal, R. López-Fonseca, R. Ferret, J.A. González-Marcos, *Appl. Catal. B: Environ.* 24 (2000) 33–43.
- [31] R. López-Fonseca, A. Aranzabal, J.I. Gutiérrez-Ortiz, J.I. Álvarez-Uriarte, J.R. González-Velasco, *Appl. Catal. B: Environ.* 30 (2001) 303–313.
- [32] Y.I. Jang, H.F. Wang, Yet-M. Chiang, *J. Mater. Chem.* 8 (1998) 2761–2764.
- [33] F. Morales, D. Grandjean, A. Mens, F.M.F. de Groot, B.M. Weckhuysen, *J. Phys. Chem. B* 110 (2006) 8626–8639.
- [34] J.L. Martin de Vidales, E. Vila, R.M. Rojas, O. Garcia-Martinez, *Chem. Mater.* 7 (1995) 1716–1721.
- [35] E. Rios, P. Chartier, J.L. Gautier, *Solid State Sci.* 1 (1999) 267–277.
- [36] V.G. Hadjiev, M.N. Iliev, I.V. Vergilov, *J. Phys. Solid State Phys. C* 21 (1988) L199–L201.
- [37] Z.Y. Tian, P.H.T. Ngamou, V. Vannier, K. Kohse-Höinghaus, N. Bahlawane, *Appl. Catal. B: Environ.* 117–118 (2012) 125–134.
- [38] J.L. Gautier, E. Rios, M. Gracia, J.F. Marco, J.R. Gancedo, *Thin Solid Films* 311 (1997) 51–57.
- [39] T.J. Chuang, C.R. Brundle, D.W. Rice, *Surf. Sci.* 59 (1976) 413–429.
- [40] J.L. Gautier, R. Fuentealba, C. Cabezas, *Z. Phys. Chem. N.F.* 126 (1981) 7.
- [41] F. Larachi, J. Pierre, A. Adnot, A. Bernis, *Appl. Surf. Sci.* 195 (2002) 236–250.
- [42] S. Hamoudi, F. Larachi, A. Adnot, A.H. Sayari, *J. Catal.* 185 (1999) 333–344.
- [43] F. Calle-Vallejo, N.G. Inoglu, H.-Y. Su, J.I. Martínez, I.C. Man, M.T.M. Koper, J.R. Kitchin, J. Rossmeisl, *Chem. Sci.* (2013) 1245–1249.
- [44] S. Ponce, M.A. Pena, J.L.G. Fierro, *Appl. Catal. B* 24 (2000) 193.
- [45] Y. Zhang-Steenwinkel, J. Beckers, A. Bliek, *Appl. Catal. A* 235 (2002) 79.
- [46] J.Y. Luo, M. Meng, X. Li, X.G. Li, Y.Q. Zha, T.D. Hu, Y.N. Xie, J. Zhang, *J. Catal.* 254 (2008) 310–324.
- [47] Q. Liang, K.D. Chen, W.H. Hou, Q.J. Yan, *Appl. Catal. A: Gen.* 166 (1998) 191–199.
- [48] F. Kapteijn, L. Singoredjo, A. Andreini, J.A. Moulijn, *Appl. Catal. B: Environ.* 3 (1994) 173–189.
- [49] X.F. Tang, Y.G. Li, X.M. Huang, Y.D. Xu, H.Q. Zhu, J.G. Wang, W.J. Shen, *Appl. Catal. B: Environ.* 62 (2006) 265–273.
- [50] X. Xie, W. Shen, *Nanoscale* 1 (2009) 50–60.
- [51] B. de Rivas, R. López-Fonseca, C. Jiménez-González, J.I. Gutiérrez-Ortiz, *J. Catal.* 281 (2011) 88–97.
- [52] A. Torncrona, M. Skoglundh, P. Thorrmahlen, E. Fridell, E. Jobson, *Appl. Catal. B: Environ.* 14 (1997) 131–146.
- [53] H. Huang, Q.G. Dai, X.Y. Wang, *Appl. Catal. B: Environ.* 158–159 (2014) 96–105.
- [54] C. Li, K. Domen, K.-i. Maruya, T. Onishi, *J. Am. Chem. Soc.* 111 (1988) 1541–1542.
- [55] P. Li, C. He, J. Cheng, C.Y. Ma, B.J. Dou, Z.P. Hao, *Appl. Catal. B: Environ.* 101 (2011) 570–579.
- [56] X.Y. Wang, Q. Kang, D. Li, *Catal. Commun.* 9 (2008) 2158–2162.
- [57] S.D. Krishnamoorthy, J.A. Rivas, M.D. Amiridis, *J. Catal.* 193 (2000) 264–272.
- [58] B.H. Aristizábal, C. Montes de Correa, A.I. Serykh, C.E. Hetrick, M.D. Amiridis, *Microporous Mesoporous Mater.* 112 (2008) 432–440.
- [59] Q. Dai, G.N. Robinson, A. Freedman, *J. Phys. Chem. B* 101 (1997) 4940–4948.
- [60] M.A. Larrubia, G. Busca, *Appl. Catal. B* 39 (2002) 343–352.
- [61] J. Lichtenberger, M.D. Amiridis, *J. Catal.* 223 (2004) 296–308.
- [62] C.E. Hetrick, F. Patcas, M.D. Amiridis, *Appl. Catal. B: Environ.* 101 (2011) 622–628.
- [63] F. Bertinchamps, A. Attianese, M.M. Mestdagh, E.M. Gaigneaux, *Catal. Today* 112 (2006) 165–168.
- [64] R.W. van den brink, R. Louw, P. Mulder, *Appl. Catal. B: Environ.* 25 (2000) 229–237.
- [65] R.W. van den brink, R. Louw, P. Mulder, *Appl. Catal. B: Environ.* 16 (1998) 219–226.
- [66] Y. Dai, X.Y. Wang, Q.G. Dai, D. Li, *Appl. Catal. B: Environ.* 111–112 (2012) 141–149.
- [67] Y. Liu, M.F. Luo, Z.B. Wei, Q. Xin, P.L. Ying, C. Li, *Appl. Catal. B: Environ.* 29 (2001) 61–67.
- [68] B.D. Rivas, R. López-Fonseca, C. Jiménez-González, J.I. Gutiérrez-Ortiz, *J. Catal.* 281 (2011) 88–97.
- [69] H. Shaw, Y. Wang, T.-C. Yu, A.E. Cerkanowicz, *ACS Symp. Ser.* 518 (1993) 358–379.
- [70] S. Krishnamoorthy, J.P. Baker, M.D. Amiridis, *Catal. Today* 40 (1998) 39–46.
- [71] M. Nagao, Y. Suda, *Langmuir* 5 (1989) 42–50.
- [72] Y. Liu, W.C. Wu, Y.J. Guan, P.L. Ying, C. Li, *Langmuir* 18 (2002) 6229–6232.
- [73] P.S. Chintawar, H.L. Greene, *J. Catal.* 165 (1997) 12–21.